

In Situ Growth of Highly Porous Zeolitic-Imidazolate Frameworks-8 on Copolymer Derived Carbon for High-Performance Supercapacitor

Pinky Saharan, Mandeep Singh, Chandan Kumar, Shashank Sundriyal,* and Sanjay R. Dhakate*

Zeolitic-imidazolate frameworks (ZIFs) are gaining widespread attention in energy storage research owing to their high porosity, structure tailorability, and multiple reaction sites. However, their very low inherent electrical conductivity limits their pristine usage in supercapacitors. Therefore, a promising way is to integrate ZIFs with suitable conductive materials, which can help to provide additional conductive pathways, thereby promoting fast charge transfer. In this work, a strategy is proposed to improve the conductivity of ZIF-8 by incorporating it with PANI-PPy conducting copolymer-derived carbon (CoP@C). The prepared ZIF-8/CoP@C composite possesses nitrogen units (pyridinic-N, graphitic-N, and pyrrolic-N) that enhance its electronic conductivity and provide additional

pseudo-capacitance. In a three-electrode setup with 1 M H₂SO₄ electrolyte, the ZIF-8/CoP@C composite electrode demonstrated the highest specific capacitance of 247.9 F g⁻¹, which is much higher than the pristine ZIF-8 electrode (72.1 F g⁻¹) at 1 A g⁻¹. Furthermore, the ZIF-8/CoP@C electrodes were employed to construct an aqueous symmetrical supercapacitor that delivers a high energy density of 25.7 Wh kg⁻¹ and a power density of 402.1 W kg⁻¹, along with prolonged cyclic stability of 92.9% after 10 000 charge-discharge cycles. This study introduces a benchmark for employing conducting copolymers to elevate the electrochemical performance of different ZIFs/MOFs in supercapacitors.

1. Introduction

With the increasing global energy consumption, the depletion of traditional fossil fuels, such as petroleum, natural gas and coal, is accelerating, leading to imminent and severe environmental consequences.^[1,2] This scenario underscores the need to develop

clean, safe, and abundant renewable energy sources. However, harnessing these renewable energies efficiently necessitates advanced energy storage systems. Over the past three decades, research has been directed toward modern electrochemical storage systems, particularly supercapacitors (SCs) and batteries. However, batteries often suffer from low cycle stability while offering high energy density (E.D.), limiting their long-term efficiency. On the other hand, SCs, characterized by their higher power density (P.D.) and excellent cyclic stability, present a promising alternative, albeit with moderate E.D.^[3–6] Efforts to develop advanced electrode materials are fundamental for boosting the overall efficiency of SCs, particularly in terms of E.D., and they are of paramount importance. Addressing this challenge is crucial for the development of next-generation SCs, which will have a pivotal impact on the future of sustainable energy storage solutions.

Zeolitic-imidazolate frameworks (ZIFs), a recently developed class of crystalline porous materials, fall under the broader category of metal-organic frameworks (MOFs) that combine the favorable properties of both MOFs and ZIFs.^[7–9] ZIFs are gaining a lot of attention in the fields of drug delivery, sensing, water purification, gas purification, and catalysis, attributable to their significant specific surface area (SSA) and large micropore volume.^[10–12] ZIFs are rarely explored as such (pristine ZIF) without any modification in energy storage, despite higher SSA, large micropore volume, and tunable pore size due to their low conductivity, which renders them ineffective in charge transfer to the current collector.^[13–15] Despite the inherent challenge of poor conductivity in these materials, the high SSA of ZIFs has driven research into their electrochemical properties and potential use as

P. Saharan, M. Singh, C. Kumar, S. R. Dhakate
Advanced Carbon Products and Metrology Department
CSIR-National Physical Laboratory (CSIR-NPL)
New Delhi 110012, India
E-mail: dhakate@nplindia.org

P. Saharan, S. R. Dhakate
Academy of Scientific and Innovative Research
Ghaziabad 201002, India

P. Saharan
School of Science
RMIT University
Melbourne, Victoria 3000, Australia

S. Sundriyal
Regional Center of Advanced Technologies and Materials
The Czech Advanced Technology and Research Institute (CATRIN)
Palacký University Olomouc
Šlechtitelů 27, 779 00 Olomouc, Czech Republic
E-mail: shashank.sundriyal@ddn.upes.ac.in

S. Sundriyal
Electrical Cluster
School of Advanced Engineering
UPES
Dehradun, Uttarakhand 248007, India

 Supporting information for this article is available on the WWW under <https://doi.org/10.1002/batt.202500477>

electrode materials for SCs. By incorporating ZIFs with other carbon materials, i.e., carbon nanotubes (CNT), graphene, conducting polymers (CPs), activated carbons, and so forth, this major constraint (poor electrical conductivity) can be overcome.^[16–21] Electrically conductive composites with ZIFs have a distinct advantage over other electrode materials like pristine graphene, CNTs, and derived carbons. This advantage stems from their high SSA characteristic, which is primarily due to the presence of ZIFs.^[8] The combination of conductivity and high SSA makes them more effective electrode materials for energy storage.

Researchers have been working to enhance the capacitance capabilities of ZIFs in energy storage devices. Akram et al. explored the electrochemical characteristics of the ZIF-67/rGO composite, finding a specific capacitance of 210 F g^{-1} at a current density of 1 A g^{-1} in a 6 M KOH electrolyte, much higher than the pristine ZIF-67.^[22] Using the direct ultrasonication technique, Wei et al. obtained nanocomposites of ZIF-8/GO and ZIF-67/GO, which exhibited specific capacitances of 400 and 252 F g^{-1} , respectively.^[21] Donghua et al. synthesized a high-specific surface nanocomposite by pyrolyzing ZIF-8/polypyrrole nanotubes and studied its electrochemical performance. This nanocomposite delivered an E.D. and P.D. of 8.42 Wh kg^{-1} and 250 W kg^{-1} simultaneously.^[23] Due to their combined improved properties, such as a large SSA, electrical conductivity, and redox activity, ZIF-carbon composites have the potential to enhance the stability and effectiveness of SCs. Therefore, ongoing research is focused on synthesizing composite materials that incorporate ZIFs with carbon materials to further enhance their electrochemical performance.

Over the past few decades, substantial research has aimed at advancing various carbon materials, particularly heteroatom-doped carbons derived from CPs. These materials are gaining significant attention due to their unique composition, which includes nonmetallic elements and strategically incorporated heteroatoms. This characteristic is crucial for developing heteroatom-doped carbon materials without metals, synthesized via *in situ* carbonization of CP.^[24,25] This approach allows for the uniform incorporation of heteroatoms into the carbon framework, unlike conventional techniques employed, including nitrogen plasma treatment, chemical vapor deposition, arc discharge, and annealing with ammonia (NH_3). The direct carbonization of CPs offers a more accessible and less harsh route to achieve desired material characteristics.^[26] Polymer-derived carbons offer heteroatom-doping, and thus these materials have emerged as a favored option for supercapacitor electrodes because of their beneficial characteristics. Their appeal stems from several factors, including their cost-effectiveness, adjustable surface chemistry, eco-friendliness, excellent electrical conductivity, high SSA, good chemical stability, rapid charge transfer kinetics, and improved wettability of the electrode material with the electrolyte.^[27] In this investigation, we explored the use of N-enriched carbon material obtained from PANI-PPy copolymer (denoted as CoP@C) as a carbon source for developing a composite material. Copolymer materials synthesized from two or more monomers exhibit synergistic effects that significantly improve both electrochemical and mechanical properties compared to their homopolymer counterparts.^[28] When converted into porous carbon, these copolymers

offer several additional advantages, including tunable pore structure, large SSA, high electrical conductivity, excellent chemical stability, and environmental sustainability.^[29,30] The selection of the PANI-PPy copolymer in this study is based on prior literature reports, which highlight its synergistic properties and potential for enhanced electrochemical performance. PANI-PPy integrates the advantageous features of both PANI and PPy.^[31] When copolymerized, the resulting copolymer-derived carbon shows improved electrochemical performance, enhanced redox-active surface sites, enhanced SSA, and better cycling durability compared to the homopolymer part.^[32,33] Furthermore, the abundant nitrogen functionalities present in the CoP@C structure can serve as nucleation sites, facilitating ZIF-8 growth.

The focus of this study is the synthesis and evaluation of a composite of ZIF-8/CoP@C, which, as per our knowledge, has not been previously reported. The incorporation of CoP@C into ZIF-8 significantly enhances the conductivity of the composite while preserving its intrinsic properties of high porosity and SSA. The ZIF-8/CoP@C composite demonstrated a notable improvement in electrochemical performance, i.e., the material achieved a specific capacitance of 247.9 F g^{-1} at 1 A g^{-1} , considerably higher than the capacitance of the pristine ZIF-8 electrode (72.1 F g^{-1}). Furthermore, the composite material was utilized to fabricate an aqueous symmetrical supercapacitor that exhibited impressive E.D. and P.D. values of 25.7 Wh kg^{-1} and 402.1 W kg^{-1} , respectively. Upon completing 10 000 charge-discharge cycles, the supercapacitor maintained a high-capacity retention of 92.9%, demonstrating its excellent stability and performance.

2. Experimental Section

2.1. Materials

2-Methylimidazole (2-Melm), aniline, pyrrole, zinc nitrate hexahydrate ($\text{Zn}(\text{NO}_3)_2 \cdot 6\text{H}_2\text{O}$), *N*-methyl-2-pyrrolidone (NMP), ferric chloride hexahydrate ($\text{FeCl}_3 \cdot 6\text{H}_2\text{O}$), methanol, sulfuric acid (H_2SO_4), and polyvinylidene fluoride (PVDF).

2.2. ZIF-8 Synthesis

For the synthesis of ZIF-8, a solution was prepared by dispersing 0.585 g of $\text{Zn}(\text{NO}_3)_2 \cdot 6\text{H}_2\text{O}$ in 20 mL of methanol, marked as X. In another beaker, 1.3 g of 2-Melm was suspended in 40 mL of methanol and marked as Y. Then, Y was added dropwise into X with constant stirring. Later, the mixture was left for 24 h. The obtained mixture was centrifuged and washed using deionized (DI) water, followed by ethanol several times. The resulting white product was oven-dried overnight at 60°C .

2.3. Synthesis of PANI-PPy Copolymer

By using $\text{FeCl}_3 \cdot 6\text{H}_2\text{O}$ as an oxidizing agent, the PANI-PPy copolymer was synthesized at room temperature using *in situ* chemical oxidative polymerization. 80 mL of DI water was used to dissolve 6 g of $\text{FeCl}_3 \cdot 6\text{H}_2\text{O}$. The resulting solution was then progressively

added to the 0.8 mL pyrrole and aniline mixture. The solution turned black after being stirred for a while, and it was then left undisturbed for 6 h at room temperature. The product was centrifuged and repeatedly cleaned using acetone and DI water. The product was then dried for 12 h at 60 °C.^[34,35]

2.4. Carbon Material (CoP@C) Synthesis from PANI-PPy Copolymer

The resulting copolymer was heated at a rate of 5 °C min⁻¹ for two hours at 800 °C to carbonize it and to obtain CoP@C.

2.5. Synthesis of ZIF-8/CoP@C Composite

Briefly, 0.1 g of CoP@C was mixed with 20 mL of methanol and was ultrasonicated for 1 h. The resultant dispersion was mixed with 0.585 g of Zn (NO₃)₂·6H₂O and stirred for 30 min (X). While 1.3 g of 2-Melm was suspended in 40 mL of methanol under stirring (Y). Y was added dropwise into X and was continuously stirred for one hour. Following this, the mixture is left undisturbed for 24 h. ZIF-8/CoP@C mixture was centrifuged, washed with water and methanol, and then dried. Figure 1 illustrates the synthesis route of the composite material.

2.6. Characterizations

The structural composition of the sample was confirmed by characterizing it with powder X-ray diffraction analysis, (Rigaku

Miniflex II Diffractometer) using Cu- κ radiation source. The analysis was performed within a diffraction angle (2θ) from 5° to 50° at a rate of 0.02° min⁻¹. The Brunauer-Emmett-Teller-SSA and pore size distribution (PSD) of the material were determined through N₂ adsorption-desorption isotherm and, Barrett-Joyner-Halenda (BJH) PSD analysis which was carried out using a Quantachrome ASIQwin (ASIQM0000-4) instrument. To assess the degree of defects and crystallinity in the sample, Raman spectra were acquired using a Renishaw (InVia) instrument with a laser wavelength of 514 nm. Finally, the elemental composition and morphology of the sample were studied using energy-dispersive spectroscopy (EDAX, OCTANE ELECT SUPER), field emission scanning electron microscope (FE-SEM, TESCAN MAGNA GMH), and transmission electron microscope (TEM, JEOL JEM-2100F). X-ray photoelectron spectroscopy (XPS) was used to analyze the chemical interactions between elements. XPS data were acquired on a Multi Lab 2000 spectrometer (Thermo Electron Corporation, England) with an Al Ka X-Ray source, featuring radiation energy of 1485.6 eV, pass energy of 55 eV, and a step size of 0.05 eV. The contact angle measurements were performed using a Krüss DSA25S drop shape analyzer with 5 μ L DI water droplets as the probe liquid.

2.7. Electrochemical Measurements

The electrochemical performance was assessed with the help of an electrochemical workstation (Biologic, Germany). The three-electrode electrochemical system is configured with a platinum wire (Pt) as the counter electrode and an Ag/AgCl reference

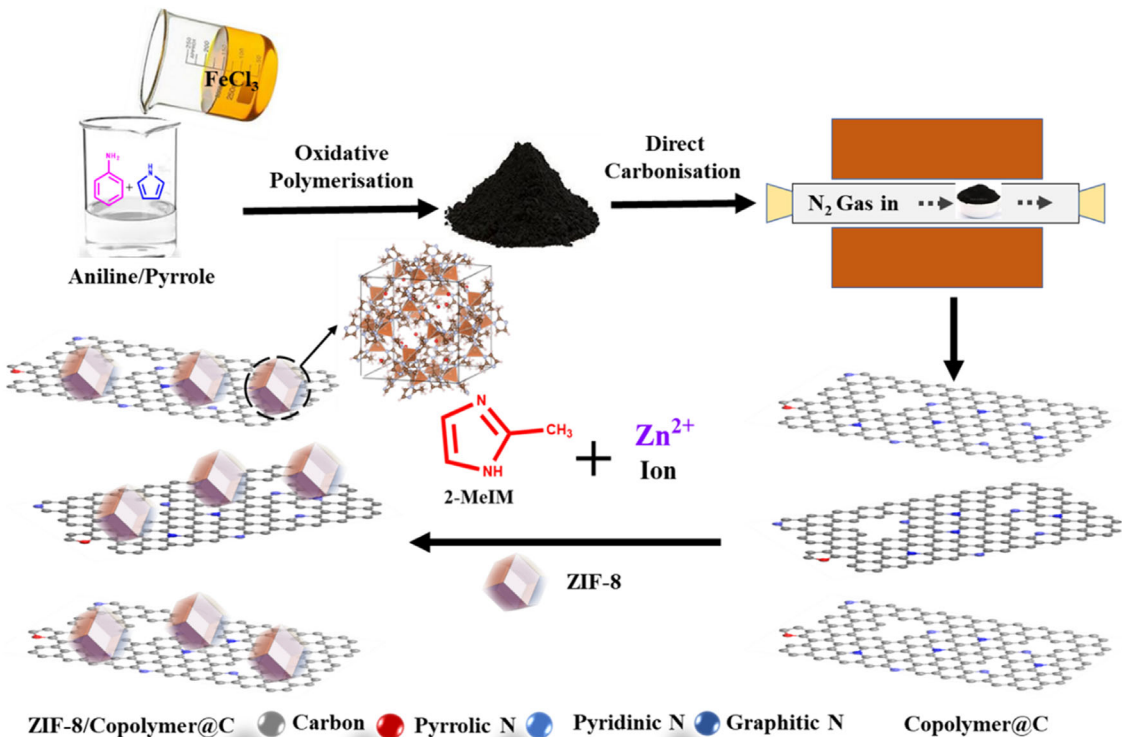


Figure 1. Schematic for the synthesis of ZIF-8/CoP@C composite.

electrode (CoP@C, ZIF-8, and ZIF-8/CoP@C) as the working electrodes, respectively. The active material was mixed with PVDF (9:1) to prepare working electrodes using NMP as a solvent. We fabricated the electrode material using the method outlined in our earlier publication.^[35] For the fabrication of working electrodes, the slurry was applied onto a graphite sheet ($3 \times 1 \text{ cm}^2$) using a drop-casting technique, achieving a mass loading of $\approx 1 \text{ mg cm}^{-2}$. Afterward, the electrodes were dried in an oven at 60°C overnight. The electrochemical behaviour of the working electrode was examined in 1 M H_2SO_4 through galvanostatic charge–discharge (GCD), cyclic voltammetry (CV), and electrochemical impedance spectroscopy (EIS). CV tests were carried out at scan rates ranging from 5 to 100 mV s $^{-1}$ between 0–1 V. EIS measurements were conducted across a frequency spectrum from 0.1 Hz to 100 kHz, using an AC signal of 10 mV. GCD measurements were performed at various current densities (0.5, 1, 2, 3, 5, and 10 A g $^{-1}$), within the same potential range of 0–1 V. The relevant calculations were based on Equation (S1) and (S2), Supporting Information, as detailed in the Supplementary Information (SI).

The practical efficacy of the electrode was subjected to a comprehensive evaluation in a two-electrode configuration employing a 1 M H_2SO_4 aqueous electrolyte, where ZIF-8/CoP@C works as both a positive and negative electrode. To fabricate a symmetrical supercapacitor device, the electrodes and the filter paper were thoroughly soaked in a 1 M H_2SO_4 electrolyte. The fabrication process involved placing filter paper between two electrodes and enclosing it with paraffin film for added mechanical strength. This was done to prevent any short circuits within the device. The assembled symmetric device was named—ZIF-8/CoP@C//ZIF-8/CoP@C. Using Equation (S3) and (S4), Supporting Information, the specific capacitance (C_s) for the device was determined. Equation (S5) and (S6), Supporting Information were used to compute the device's E.D. and P.D.

3. Results and Discussion

3.1. Structural and Morphological Studies

To determine the structural parameters of all the materials, X-ray diffraction (XRD) and Raman analysis were conducted. Figure 2a

represents the XRD spectra of ZIF-8, CoP@C, and ZIF-8/CoP@C. In the XRD spectrum of CoP@C, two broad peaks around $2\theta \approx 24.5^\circ$ and 43.3° represent the (002) and (101) crystal planes of carbon, respectively.^[36] A broader peak width reveals the turbostratic nature of carbon.^[37] The XRD spectra of ZIF-8 show intense and sharp diffraction peaks, which suggest the crystalline nature of the sample. The product is determined to be a single-phase ZIF-8 structure, confirmed with the previously reported ZIF-8 spectrum from the literature.^[38,39] Furthermore, we have analyzed the ZIF-8 data using XPert-High score software, and it has been observed that the characteristic peak of ZIF-8 matches the standard (JCPDS no: 00-062-1031) reference of ZIF-8, indicating the formation of pure ZIF-8. Hereafter, average crystallite size and d-spacing were estimated using the Debye-Scherrer equation and Bragg's equation for pure ZIF-8 and ZIF-8/CoP@C composite. It has been seen that ZIF-8 and ZIF-8/CoP@C show average crystallite size of 41.9 and 46.2 nm, respectively.^[40] The results indicate that the slight increase in average crystallite size could be attributed to the incorporation of CoP@C, which promotes an increase in crystallite size and signifies the enhanced growth of ZIF-8 nanoparticles on the CoP@C interface. The ZIF-8/CoP@C material exhibits a pattern that is identical to that of the pristine ZIF-8 with no discernible loss of crystallinity, proving that the crystalline structure of ZIF-8 was neither disrupted nor destroyed by the introduction of carbon. Due to the low concentration of CoP@C or high dispersion in the composite, the ZIF-8/CoP@C only exhibits the representative characteristic peaks of ZIF-8. The diffraction peak intensity of carbon is too weak in the ZIF-8/CoP@C composite in comparison to that of the ZIF-8 polyhedra.^[22,41]

Raman spectroscopy has been implemented for the measurement of the vibrational modes of the samples (Figure 2b) over a spectral region of 150–2000 cm $^{-1}$. The Raman spectra for the synthesized ZIF-8 are consistent with the existing literature.^[42] In the Raman spectra of CoP@C, two bands, at 1353 cm $^{-1}$ (D) and 1588 cm $^{-1}$ (G), are observed.^[43] In the ZIF-8/CoP@C, notable peaks corresponding to ZIF-8 appear alongside distinct carbon bands, namely the D band at 1337 cm $^{-1}$ and the G band at 1583 cm $^{-1}$, respectively, which indicate the presence of both

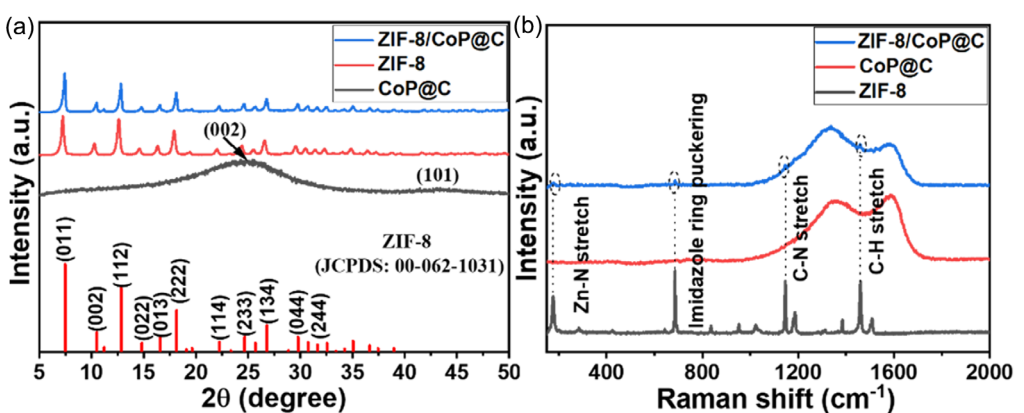


Figure 2. a) XRD, and b) Raman spectrum of ZIF-8, CoP@C and ZIF-8/CoP@C.

carbon and ZIF-8 in the composite. CoP@C exhibits an I_D/I_G ratio of 0.95, while for the ZIF-8/CoP@C the ratio has been increased to 1.08, which indicates the incorporation of ZIF-8 in the composite.^[44–46] The increased I_D/I_G ratio for the ZIF-8/CoP@C composite arises from the *insitu* growth of ZIF-8 nanocrystals on CoP@C. This introduces additional structural defects at the carbon-ZIF-8 interface.^[47–50] These defects may provide more active sites for charge storage and facilitate rapid ion transport, thereby enhancing the specific capacitance and overall electrochemical performance of the electrode.^[51,52]

The morphology of ZIF-8, CoP@C, and ZIF-8/CoP@C was examined using FE-SEM. FE-SEM analysis of CoP@C reveals an agglomerated quasispherical structure depicted in Figure S1a,b, Supporting Information (SI). ZIF-8 possesses a crystalline morphology having a rhombic dodecahedron structure (Figure 3a,b).^[53] From Figure 3c,d, it is evident that the CoP@C's quasispheres and ZIF-8's crystal are evenly distributed well with the ZIF-8/CoP@C composite. EDS analysis further reveals the presence of Zn, confirming the existence of ZIF-8 in the composite.

Further analysis of the microstructure and morphology of the ZIF-8/CoP@C composite was performed using TEM. Figure 4a–c illustrates the TEM images of the ZIF-8/CoP@C composite. CoP@C possesses agglomerated spherical morphology, observed via FE-SEM analysis (Figure S1a,b, Supporting Information), while in the composite, these spheres are well distributed within ZIF-8 crystals. One or more ZIF-8 crystals can be seen connected by CoP@C. This can also be seen from TEM images that the addition of CoP@C does not distort the structure and skeleton of ZIF-8, which is consistent with that of the XRD spectra. HR-TEM image of ZIF-8/CoP@C (Figure 4d) also shows the presence of crystalline fringes. CoP@C is amorphous, as confirmed by XRD data, so the observed crystalline fringes are attributed to ZIF-8 within

the composite, supporting the formation of the ZIF-8/CoP@C composite.

XPS analysis is also performed on the prepared samples to probe the chemical states of the constituent elements. Figure 5 depicts the XPS spectrum of ZIF-8 and ZIF-8/CoP@C. The survey scan for the ZIF-8 composite affirms the presence of four elements, namely C, Zn, O, and N (Figure 5a). The survey scan spectra of CoP@C are depicted in SI as Figure S2a, Supporting Information, confirming the existence of only C, O, and N. The survey scan spectra of ZIF-8/CoP@C are consistent with those of ZIF-8,^[54,55] suggesting the successful growth of ZIF-8 within the composite. Zn 2p spectra displayed in Figure 5b demonstrate two highly prominent peaks at ≈ 1021.4 and ≈ 1044.1 eV, respectively, linked to the Zn 2p_{3/2} and Zn 2p_{1/2} components.^[56] The Zn 2p spectrum observed in ZIF-8/CoP@C is consistent with that of pristine ZIF-8. The Zn 2p_{3/2} and Zn 2p_{1/2} XPS peaks of the ZIF-8/CoP@C composite display noticeable broadening and a slight shift toward lower binding energies compared to pristine ZIF-8. This shift indicates a change in the electronic environment of Zn²⁺ ions, caused by coordination with nitrogen-containing groups (pyridinic-N, pyrrolic-N, and graphitic-N) in the CoP@C. Lone-pair electrons from these nitrogen sites can coordinate with Zn²⁺, leading to a shift in binding energy and peak broadening. Thus, the peak broadening and shifting in the Zn 2p spectrum support interaction between ZIF-8 and the CoP@C, confirming chemical coupling rather than physical mixing.^[56,57] The deconvoluted C 1s spectra of ZIF-8 and ZIF-8/CoP@C are shown in Figure 5c. ZIF-8 displayed two prominent peaks at 284.4 and 285.8 eV, while ZIF-8/CoP@C exhibited peaks at 284.4 and 286.8 eV. These peaks correspond to the C=C/C≡C bonds and the C=N bond, respectively.^[58,59] The high-resolution C1s spectra of CoP@C is depicted in Figure S2b, Supporting Information. It also showed the peaks attributed to

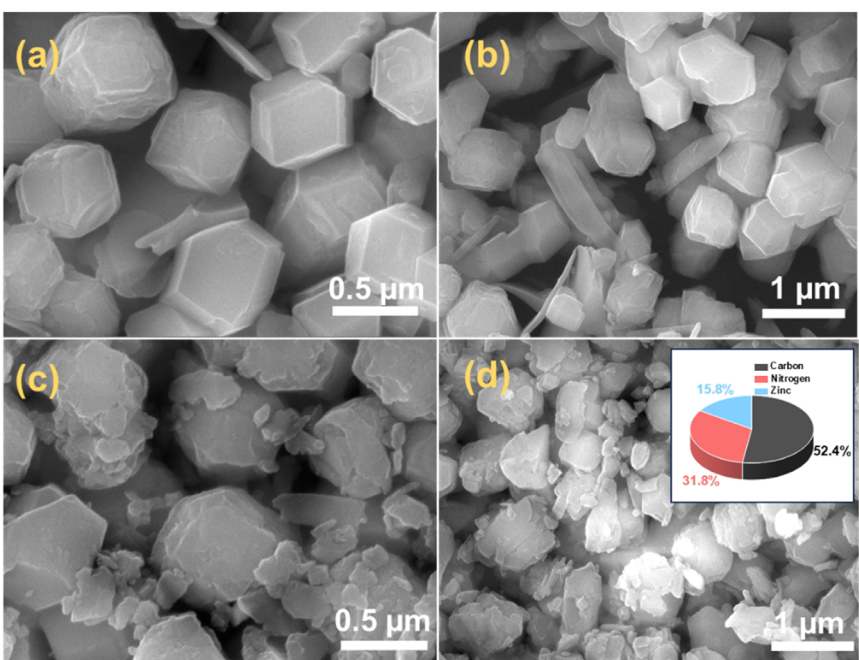


Figure 3. Morphological analysis of a,b) ZIF-8 and c,d) ZIF-8/CoP@C (Figure 3d Inset: Elemental composition using EDS analysis).

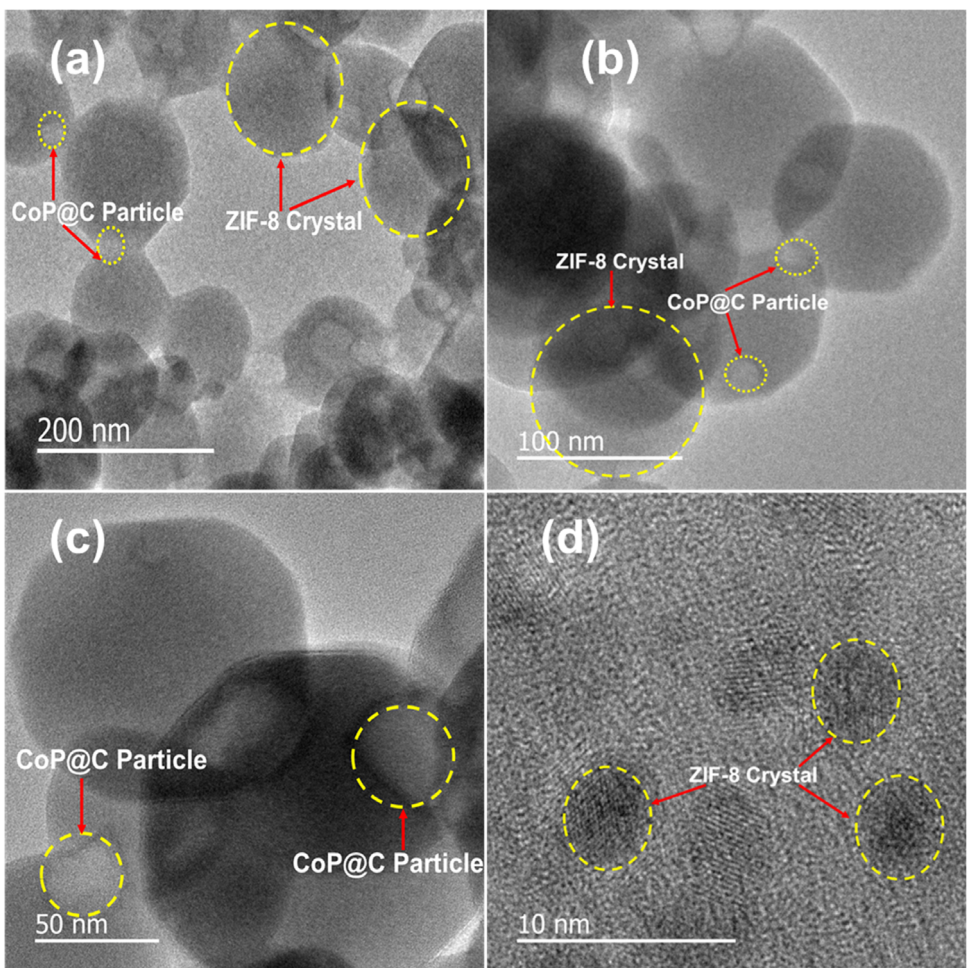


Figure 4. a–c) TEM images of ZIF-8/CoP@C, and d) HR-TEM image of ZIF-8/CoP@C.

the C—C/C=C bonds and the C—N bond. Additionally, N1s spectra of CoP@C is resolved into three peaks at binding energies of 398.2, 399.8, and 401.0 eV, linked to pyridinic-N, pyrrolic-N, and graphitic-N, as shown in Figure S2c, Supporting Information.^[26,60] Introducing nitrogen units into the carbon matrix can lead to significant disruptions in the carbon structure. Since nitrogen's atomic radius closely matches that of carbon, it is easily incorporated into the carbon lattice, reducing the risk of lattice mismatches. Moreover, nitrogen, with its greater electron density compared to carbon, acts as an electron donor, enriching the carbon network with additional electrons. Graphitic-N boosts the material's electrical conductivity, while pyridinic and pyrrolic-N, on the other hand, introduce electron-rich sites that promote pseudocapacitive behaviour.^[27,35,61] CoP@C's inherent N-doping could provide nucleation sites, facilitating the growth of ZIF-8. The deconvoluted N 1s spectrum of ZIF-8 and ZIF-8/CoP@C is provided in Figure 5d. N 1s spectra of ZIF-8 show the presence of two characteristic peaks centered at 398. and 399.8 eV affiliated with N—C and Zn—N bonding.^[62] The N 1s spectrum of ZIF-8/CoP@C displays characteristics of both ZIF-8 and CoP@C, with peaks coherent to pyridinic-N (397.9 eV), pyrrolic-N (398.8 eV), graphitic-N (400.7 eV), and Zn—N (399.5 eV). The pyrrolic-N arises both from CoP@C and from

the presence of 2-methylimidazole (acting as a ligand in ZIF-8).^[63] Hence, XPS confirms that the prepared composite possesses various nitrogen units, which help to create defects in the composite, potentially enhancing its electrochemical performance and revealing crucial insights into the chemical bonding and composition of the ZIF-8/CoP@C hybrid electrode, reinforcing the composite material's structural integrity and elemental constituents.

PSD and SSA are crucial parameters that can significantly impact the specific capacitance of materials used in SCs.^[64,65] As a result, N₂ adsorption–desorption and Barrett–Joyner–Halenda (BJH) techniques were utilized to study the samples' SSA and PSD. The isotherms for N₂ adsorption/desorption of ZIF-8, CoP@C, and ZIF-8/CoP@C are depicted in Figure 6a. The SSA for ZIF-8, CoP@C, and ZIF-8/CoP@C was assessed as 1448.1, 329.5, and 1209.7 m² g⁻¹, respectively summarized in Table 1. The SSA of the ZIF-8/CoP@C is lowered compared to ZIF-8, due to the introduction of less porous CoP@C. However, still ZIF-8/CoP@C has an SSA of ≈3.7 times exceeding CoP@C. The total pore volume of ZIF-8/CoP@C is 0.58 cc g⁻¹, much higher than the pristine CoP@C (0.21 cc g⁻¹). The BJH, PSD curve in Figure 6b provides a clearer insight into the mesoporous distribution of the samples. ZIF-8/CoP@C has a higher mesoporous volume compared to

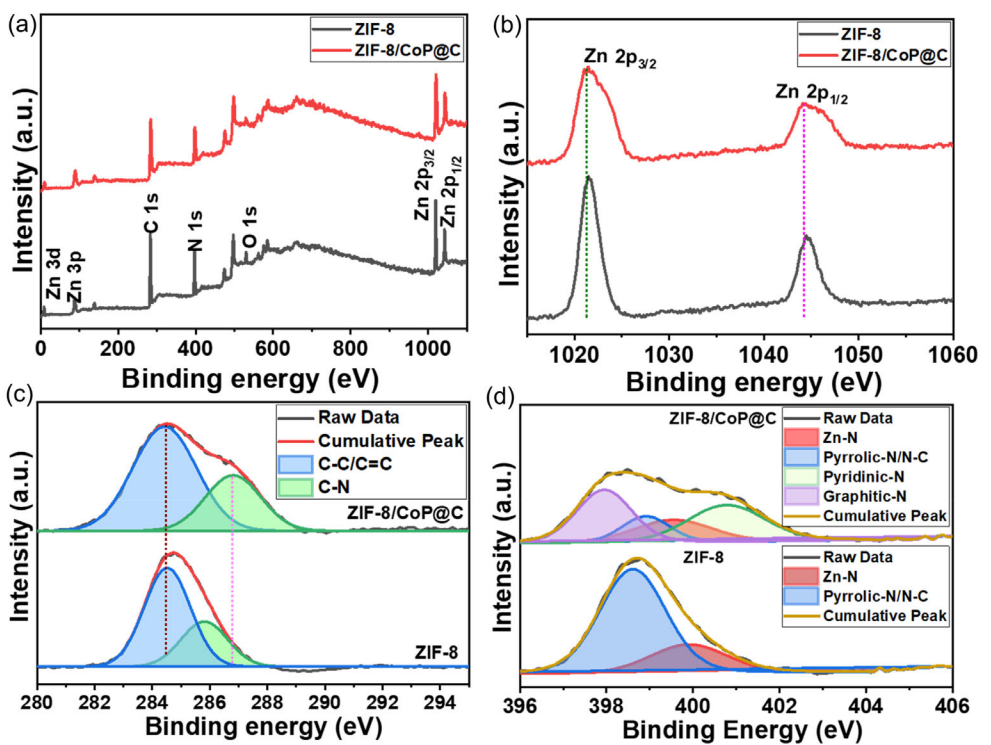


Figure 5. a) Survey scan corresponding to ZIF-8 and ZIF-8/CoP@C, deconvoluted spectra of b) Zn 2p spectra corresponding to ZIF-8 and ZIF-8/CoP@C, c) C1s, and d) N1s spectra of ZIF-8 and ZIF-8/CoP@C.

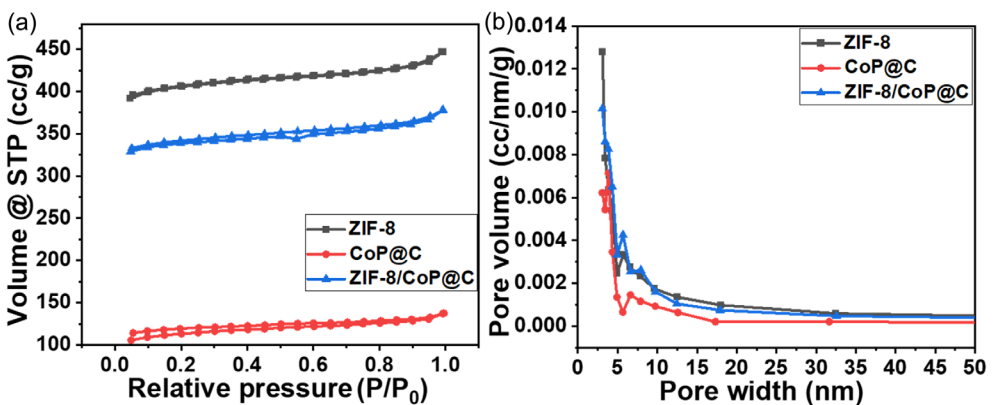


Figure 6. a) The isotherms for N_2 adsorption–desorption and b) the BJH pore size distribution curves of ZIF-8, CoP@C and ZIF-8/CoP@C.

Table 1. Comparative SSA and pore parameters of the samples.

Sample	S_{BET} [$\text{m}^2 \text{ g}^{-1}$]	Average pore diameter [nm]	V_{total} [cc g^{-1}]	V_{meso} [cc g^{-1}]	V_{micro} [cc g^{-1}]	$V_{\text{meso}}/V_{\text{micro}}$ [%]
ZIF-8	1448.1	1.91	0.69	0.066	0.624	10.6
CoP@C	329.5	2.46	0.21	0.032	0.178	17.9
ZIF-8/CoP@C	1209.7	1.94	0.58	0.065	0.515	12.6

CoP@C, which is visible in the BJH curve. The CoP@C material has high conductivity but a lower SSA. The pristine ZIF-8 lacks conductivity; however, the composite material combines the benefits of both properties. Despite introducing conductivity (CoP@C), the ZIF-8/CoP@C's SSA is not significantly compromised, which is a

significant advantage that could enhance its electrochemical performance. $V_{\text{Meso}}/V_{\text{Micro}}$ ratio is a key factor influencing ion transport and charge storage. Micropores ($< 2 \text{ nm}$) contribute mainly to electric double-layer formation, while mesopores ($2\text{--}50 \text{ nm}$) act as ion pathways that facilitate rapid electrolyte access to microporous

regions.^[66] As shown in Table 1, ZIF-8 has a low $V_{\text{Meso}}/V_{\text{Micro}}$ ratio (10.6%), indicating a micropore-dominated structure, which limits ion transport despite its high SSA. CoP@C shows a higher ratio (17.9%) with improved ion accessibility but lower SSA. The ZIF-8/CoP@C composite achieves an enhanced ratio (12.6%) with a high SSA ($1209.7 \text{ m}^2 \text{ g}^{-1}$). This pore structure, combined with good conductivity, might contribute to the composite's superior capacitance and rate performance.^[67]

The contact angle provides insight into the surface properties of the material, specifically its hydrophobicity or hydrophilicity. Figure S3a–c, Supporting Information presents the contact angle measurements for the pristine and composite electrode materials coated on a glass slide, using 5 μL DI water droplets. We prepared smooth films by drop-casting the slurry of each material onto clean glass slides under the same conditions used for electrode preparation. All three materials exhibit hydrophobic behavior, with contact angles falling within a similar range. The contact angle for ZIF-8 was measured to be 124° , indicating a predominantly hydrophobic surface. This behavior aligns with the known crystalline structure of ZIF-8, where the external surfaces may expose 2-methylimidazole linkers, which are nonpolar and thus reduce the material's affinity toward polar solvents.^[68] The CoP@C sample exhibited a slightly lower contact angle of 122° . The ZIF-8/CoP@C composite showed a contact angle of 130° , the highest among the three. The slight increase compared to the individual components suggests that the integration of ZIF-8 with CoP@C enhances the overall hydrophobicity of the composite, likely due to the combined nonpolar characteristics of both materials, which further reduce surface wettability.

3.2. Electrochemical Performance Analysis of the Electrodes

After confirming the materials synthesis, the electrodes were tested in a three-electrode electrochemical cell using GCD, CV, and EIS analysis in 1 M H₂SO₄. At the outset, CV was performed on the samples (ZIF-8, CoP@C, and ZIF-8/CoP@C) at various scan rates between 5 and 100 mV s⁻¹. Figure 7a illustrates the CV profiles of ZIF-8, CoP@C, and ZIF-8/CoP@C recorded at 10 mV s⁻¹. Among these electrodes, ZIF-8/CoP@C displays the greatest area under the curve, delivering the highest Cs of 206.8 F g^{-1} , which is considerably superior to that of CoP@C (128.1 F g^{-1}) and pristine ZIF-8 (70.1 F g^{-1}). The ZIF-8/CoP@C electrode's superior electrochemical performance is attributed to its high SSA and the presence of a conducting surface. Figure 7b additionally illustrates the CV profile for the ZIF-8/CoP@C. To assess the possible effect of the graphite current collector on the electrochemical measurements, a control experiment was carried out using a bare graphite sheet under the same experimental conditions. As depicted in Figure S4a, Supporting Information, the CV response of the blank graphite sheet shows minimal capacitive behaviour within the investigated potential window, with almost negligible current compared to electrodes containing active material. In contrast, the ZIF-8/CoP@C electrode displays a much higher current response and a significantly broader CV profile relative to both the blank and the individual active components. This clearly illustrates that the enhanced capacitive performance originates from the synergistic interaction between ZIF-8 and CoP@C, rather than from the graphite current collector itself. The CV profile of a blank graphite sheet is depicted in Figure S4b, Supporting Information.

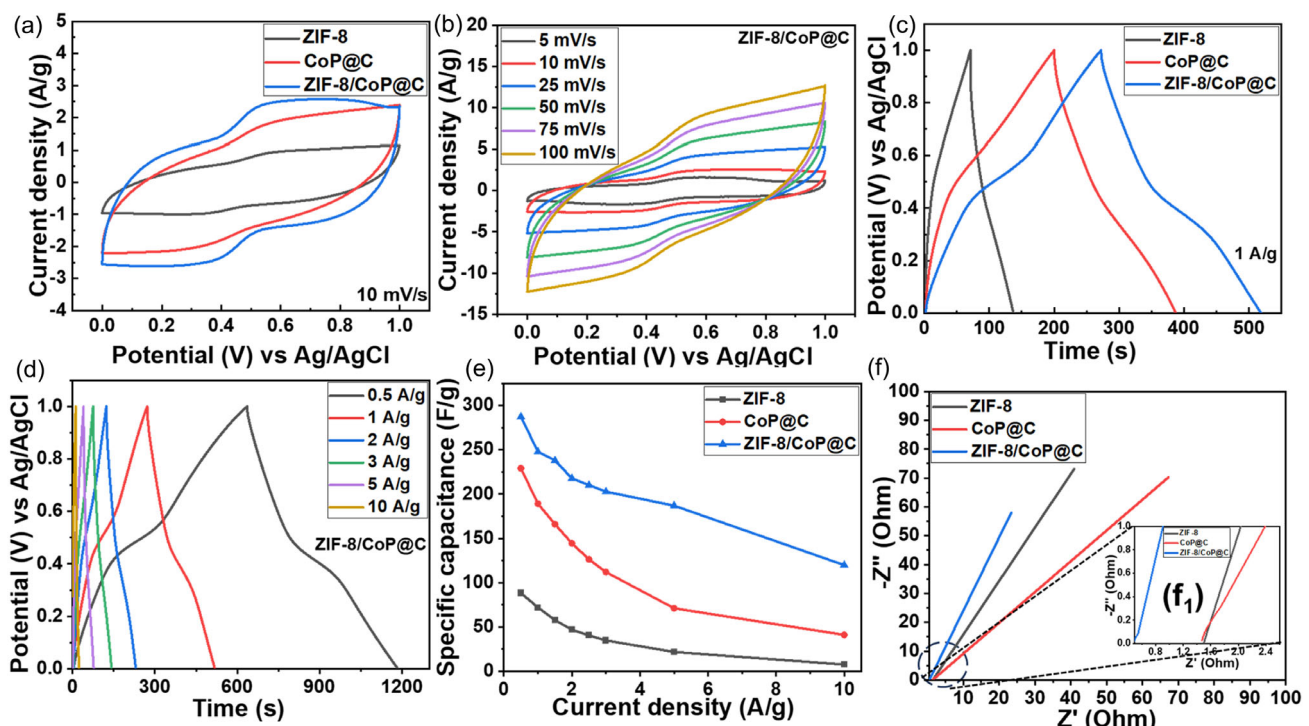


Figure 7. Electrochemical performance of the samples: a) comparison of CV curves at 10 mV s^{-1} , b) CV profiles of ZIF-8/CoP@C, c) comparative GCD curves at 1 A g^{-1} , d) GCD profiles of ZIF-8/CoP@C at varying current density, e) rate capability, and f) Nyquist plot accompanied by an enlarged view (f₁).

For reference, the CV profiles for ZIF-8 and CoP@C are provided in Figure S5a,b, Supporting Information. The decrease in electrode Cs with increasing scan rates is due to the limited time availability for electrolyte ions to engage with the accessible pores of the active electrode material at accelerated scan rates.^[69] GCD analysis was performed to assess the capacitive behaviour, and the results at 1 A g⁻¹ (current density) are illustrated in Figure 7c. Based on the GCD profile, the Cs of ZIF-8, CoP@C, and ZIF-8/CoP@C electrodes were calculated as 72.1, 189.1, and 247.9 F g⁻¹, respectively. Under lower scanning rates, the material exhibits characteristics of both electric double-layer capacitance (EDLC) and pseudocapacitive behaviour, which jointly affect the electrochemical performance of the electrodes. However, at higher scanning rates, EDLC becomes the key factor in determining the electrochemical behaviour of the material. The GCD curves for the ZIF-8/CoP@C electrode are illustrated in Figure 7d. Similarly, Figure S5c,d, Supporting Information displays the GCD curves of ZIF-8 and CoP@C electrodes.

The rate capability of the ZIF-8, CoP@C, and ZIF-8/CoP@C electrodes was evaluated by comparing their specific capacitance values at various current densities, as shown in Figure 7e. All three electrodes exhibit a gradual decrease in capacitance with increasing current density, which is expected due to limited ion diffusion and reduced charge storage time at higher rates. Among them, ZIF-8/CoP@C stands out with the highest Cs at varying current densities. Even at 10 A g⁻¹, the ZIF-8/CoP@C samples showcased a notable Cs of 119.9 F g⁻¹. This performance can be ascribed to their superior electrical conductivity and higher SSA, which together enhance rate capability and overall electrochemical performance, establishing them as a promising option for electrochemical energy storage. The long-term cycling performance of the ZIF-8, CoP@C, and ZIF-8/CoP@C electrodes was assessed over 5000 continuous charge–discharge cycles at a current density of 10 A g⁻¹. As shown in Figure S6, Supporting Information, all three electrodes show complete capacity retention throughout the cycling period. To evaluate the internal resistance of the prepared samples, the Nyquist plot is presented in Figure 7f. The equivalent series resistance (ESR), which is a vital impedance parameter, significantly contributes to the electrochemical efficacy of electrode material. Results show that ZIF-8/CoP@C demonstrates the lowest ESR compared to ZIF-8 and CoP@C. The ESR of the ZIF-8/CoP@C electrode was measured at 0.93 Ω, while the ESR values for CoP@C and ZIF-8 electrodes were 1.32 and 1.55 Ω, respectively. The reduced ESR in the ZIF-8/CoP@C electrode is due to the synergistic effect of its higher SSA and conductivity. As a result, the superior electrochemical performance of the ZIF-8/CoP@C electrode was corroborated through CV, GCD, and EIS analyses.

To gain deeper insight into the electrochemical charge storage mechanism of the ZIF-8/CoP@C composite, a kinetic study was conducted using CV. The relationship between peak current (i) and scan rate (v) was analyzed according to Equation (1), where b is the slope obtained from plotting $\log(i)$ versus $\log(v)$, indicating the charge storage mechanism type. A b -value close to 0.5 suggests a diffusion-controlled (battery-type) process, while a value near 1.0 indicates surface-controlled (capacitive) behaviour.^[70]

$$i = av^b \quad (1)$$

As shown in Figure 8a, the ZIF-8/CoP@C composite exhibits a higher b -value (0.69) compared to CoP@C (0.63) and ZIF-8 (0.64), indicating an enhanced contribution from capacitive behaviour in the composite electrode. This enhancement can be attributed to the synergistic combination of the highly porous ZIF-8 structure and the nitrogen-doped carbon derived from the PANI-PPy copolymer, which promotes efficient ion transport and abundant electroactive sites.

To quantify the specific contributions from capacitive and diffusion-controlled processes at different scan rates, the Dunn method was applied.^[71,72] Since electrode materials typically exhibit a mixture of both behaviours, the total current can be expressed as the sum of surface-controlled and diffusion-controlled components

$$i = i_s + i_d \quad (2)$$

here, i_d corresponds to the current portion limited by diffusion, while i_s corresponds to the current arising from surface-controlled mechanisms.

According to the Dunn approach, the capacitive (surface-controlled) current scales linearly with scan rate, while the diffusion-controlled current depends on the square root of the scan rate, as described by

$$i_s = K_a v \quad (3)$$

$$i_d = K_b v^{1/2} \quad (4)$$

here, K_a and K_b are proportionality constants related to the respective charge storage mechanisms.

The total current (i) can be expressed as the sum of two components: one proportional to the scan rate (v) and the other proportional to the square root of the scan rate ($v^{1/2}$), represented as

$$i = K_a v + K_b v^{1/2} \quad (5)$$

(Equation 5) represents a linear expression, where the analysis of the slope and intercept offers quantitative insights into the relative contributions of surface-controlled (capacitive) and diffusion-controlled processes. Figure 8b–d quantifies the respective surface (capacitive) and diffusion-controlled charge contributions across varying scan rates for ZIF-8, CoP@C, and ZIF-8/CoP@C, respectively. For ZIF-8 (Figure 8b), diffusion dominates charge storage at low scan rates (84.6% at 5 mV s⁻¹) due to its microporous structure limiting ion transport. However, the capacitive contribution progressively increases with scan rate, reaching ≈49.8%, reflecting surface-controlled charge storage in ZIF-8 at higher rates. CoP@C (Figure 8c) shows a similar trend, with diffusion-controlled processes composing 88.2% of the charge storage at 5 mV s⁻¹. The capacitive charge contribution for ZIF-8 grows more rapidly with increasing scan rate compared to CoP@C, indicating a higher surface-controlled charge mechanism in ZIF-8 at elevated scan rates. On the other hand, CoP@C shows a smaller increase in capacitive contribution over the same scan rate range, highlighting a

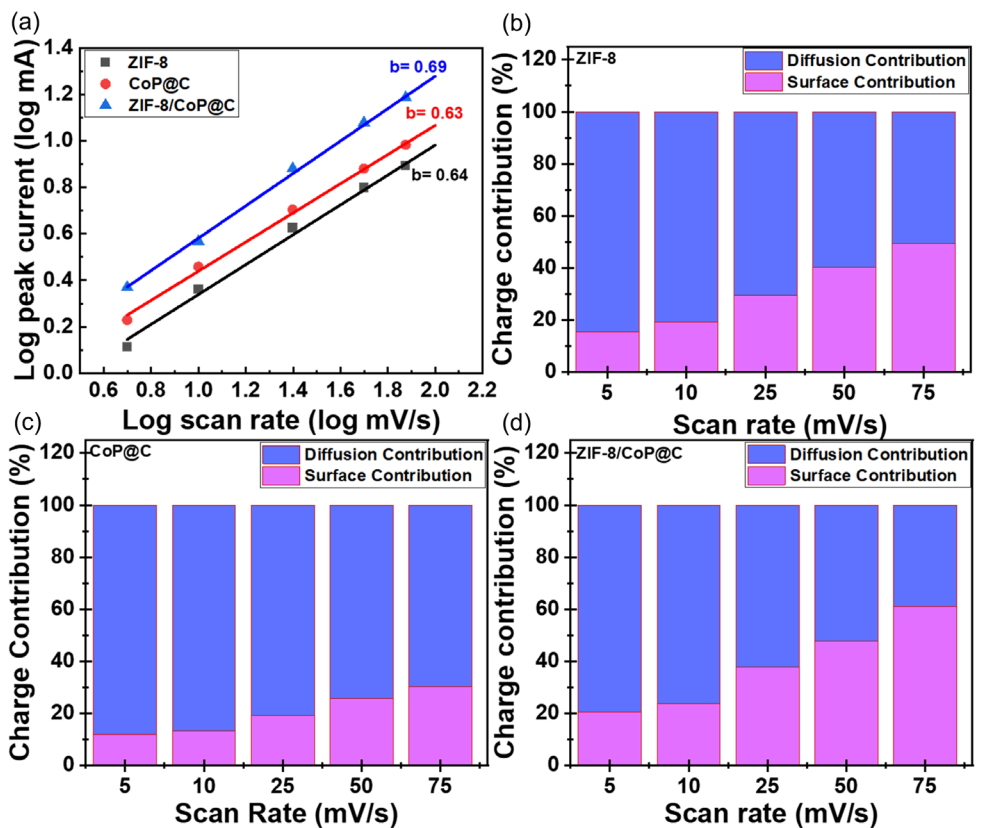


Figure 8. a) Obtained b value for ZIF-8, CoP@C and ZIF-8/CoP@C electrodes and diffusion and capacitive contribution for b) ZIF-8, c) CoP@C, and d) ZIF-8/CoP@C.

more sustained dominance of diffusion-controlled mechanisms. The ZIF-8/CoP@C composite (Figure 8d) demonstrates a marked increase in capacitive behaviour with scan rate, surpassing 60% capacitive contribution at high scan rate, indicating a higher surface-controlled charge mechanism at elevated scan rates. Hence, the charge storage mechanism for all the electrodes at a lower scan rates is diffusion-controlled, and at a high scan rate is surface-controlled.

3.3. Electrochemical Performance Study of Supercapacitor Device

The practicality of a supercapacitor electrode can be assessed through the examination of its performance in a two-electrode system. For this, the ZIF-8/CoP@C electrode was assembled in a symmetrical configuration as both the negative and positive electrodes. To determine the operating potential range for the aqueous device, the performance of the assembled device was evaluated by obtaining a CV curve at various potential windows with a consistent scan rate. The data demonstrated that the device functioned effectively within the potential window of 0–1.6 V. Figure S7a,b, Supporting Information illustrates the optimization curves for the device's potential window. For the assembled device, GCD, CV, and EIS analysis were carried out to assess their E.D., P.D. Figure 9a illustrates the CV profiles of ZIF-8/CoP@C//ZIF-8/CoP@C symmetrical SC device at spanning scan rates of 5–100 mV s⁻¹. The observed rectangular

shape in the device's CV profile is indicative of electric double-layer capacitors, reflecting the device's robust power capabilities. In addition, the GCD analysis conducted across a spectrum of current densities (0.5–10 A g⁻¹), as depicted in Figure 9b, reveals that the resulting curves remain consistently linear, regardless of whether the current densities are high or low. This consistent linearity underscores the impressive EDLC characteristics exhibited by the material. Figure 9c presents the Nyquist plot for the ZIF-8/CoP@C//ZIF-8/CoP@C device. This plot is essential for assessing the impedance characteristics of the device, providing insights into its circuit configuration. The Nyquist plot demonstrates the correlation between the imaginary and real components of the impedance, providing crucial information about charge transfer resistance and ion diffusion within the supercapacitor. The semicircle observed at higher frequencies indicates the charge transfer resistance, while the straight line at lower frequencies suggests good ion diffusion characteristics. The Nyquist plot data were analyzed using a Z-fitting function in Biologic software, allowing for a thorough investigation of the device's electrochemical performance.

The impedance characteristics of the device are detailed in Table S1, Supporting Information, which shows lower values for R_{s} and R_{ct} . The "difference parameter," labeled as "a," takes on values ranging from 0 to 1, providing insight into the performance characteristics of the supercapacitor device (Equations S7, S8, Supporting Information). When the value approaches 1, it signifies that the behaviour of the Constant Phase Element (CPE) aligns

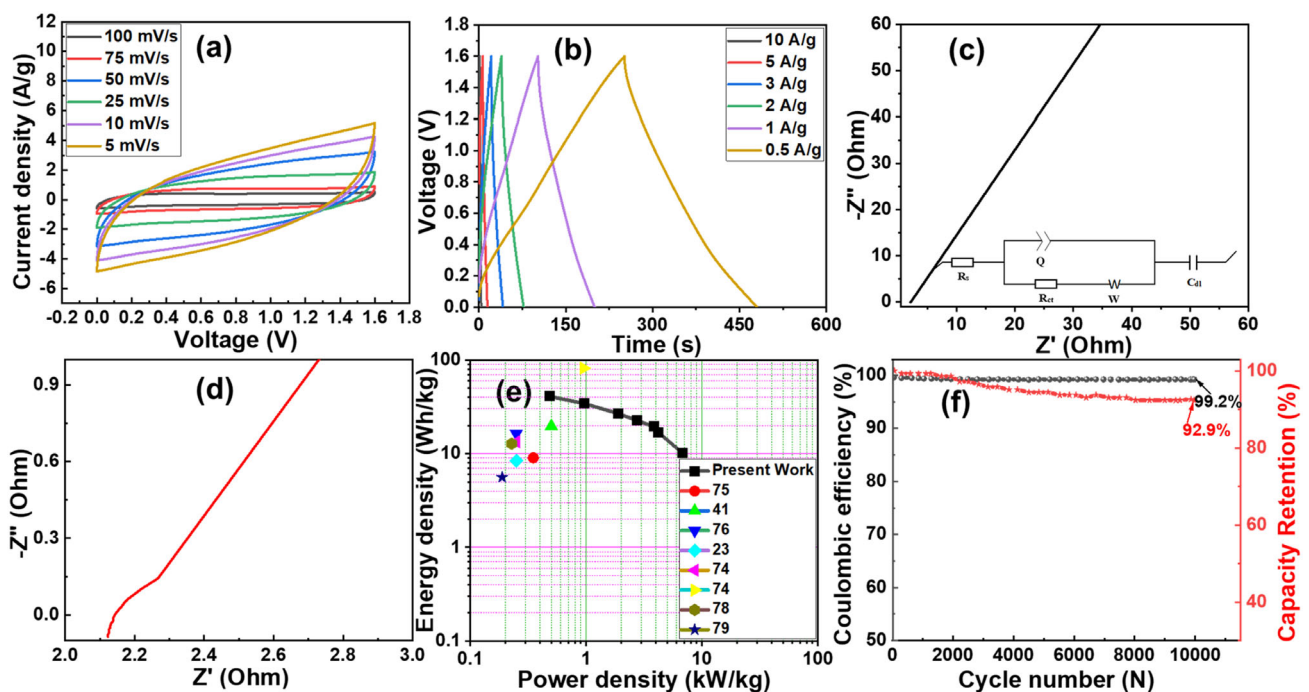


Figure 9. Electrochemical analysis of ZIF-8/CoP@C//ZIF-8/CoP@C symmetrical SC device: a) CV curve at varying scan rates, b) GCD curve at varying current density, c) Nyquist plot (Inset showing equivalent circuit), d) the high-frequency segment of the Nyquist plot, e) Ragone plot, and f) coulombic efficiency and capacitance retention versus cycle number.

closely with that of an ideal capacitor, indicating minimal deviation from perfect capacitive behaviour.^[73] Figure 9d shows a detailed view of the high-frequency area of the Nyquist plot. The Ragone plot depicted in Figure 9e effectively highlights the relationship between E.D. and P.D. for the device. The device achieves an

impressive E.D. of 25.7 Wh kg^{-1} at a P.D. of 402.1 W kg^{-1} when tested at 0.5 A g^{-1} . This performance underscores the device's ability to balance high energy storage with rapid discharge capabilities. Such characteristics are crucial for applications demanding quick energy delivery. The Ragone plot presented in Table S2,

Table 2. Assessment of electrochemical performance differences of ZIF-8/CoP@C//ZIF-8/CoP@C aqueous devices with various ZIF/carbon composite-based materials.

S. No.	Material used	Additive used	Specific capacitance [F g^{-1}] a)	Voltage window [V]	Energy density [Wh kg^{-1}]	Power density [W kg^{-1}]	Ref.
1.	ZIF-8 derived nanohexahedron carbon	–	132.8 F g^{-1} at 0.5 A g^{-1} # ^{a)}	0–1.4	9.04	350.0	[75]
2.	ZIF-67-derived phosphide	Phosphorized	55.4 F g^{-1} at 1 A g^{-1} # ^{a)}	0–1.6	19.7	500.0	[41]
3.	N-doped ZIF-8-derived carbon	Melamine doped	118.5 F g^{-1} at 1 A g^{-1} # ^{a)}	0–1.0	16.4	249.1	[76]
4.	ZIF-67 derived porous carbon/graphene composite	–	53.0 F g^{-1} at 5 mV s^{-1} # ^{a)}	0–1.0	–	–	[77]
5.	ZIF-8/polypyrrole carbon composite	KOH activated	208.8 F g^{-1} at 1 A g^{-1} # ^{a)}	0–1.0	8.4	250.0	[23]
6.	ZIF-8/polyaniline@cellulose-derived carbon aerogel	Urea/KOH	388.0 F g^{-1} at 0.5 A g^{-1} # ^{a)}	0–1.0	13.4	250.0	[74]
7.	ZIF-8/polyaniline@cellulose-derived carbon aerogel	Urea/KOH	388.0 F g^{-1} at 0.5 A g^{-1} # ^{a)}	0–3.8	81.8	950.0	[74]
8.	ZIF-8/polypyrrole/rGO	–	78.1 F g^{-1} at 1 A g^{-1} # ^{a)}	0–1.0	12.8	227.1	[78]
9.	Graphitic carbon nitride and ZIF-67	–	144.0 F g^{-1} at 1 A g^{-1} # ^{a)}	0–0.75	5.6	188.0	[79]
10.	ZIF-8 derived N, P, O-doped porous carbon	Phytic acid	219.4 F g^{-1} at 1 A g^{-1} # ^{a)}	1.0–0	–	–	[80]
11.	ZIF-8/PANI-PPy derived carbon composite	–	459.3 F g^{-1} at 0.5 A g^{-1} # ^{a)}	0–1.6	25.7	402.1	Current study

a) and # represent the electrochemical behaviour in three and two-electrode systems, respectively.

Supporting Information details the performance of the aqueous device across different current densities. Specifically, as the current density is increased from 0.5 to 2 A g⁻¹, the E.D. declines from 25.7 to 17.3 Wh kg⁻¹. In contrast, the P.D. increases significantly, going from 402.1 to 1632.4 W kg⁻¹. Additionally, the device's cyclic stability was assessed at 10 A g⁻¹, where it maintained an impressive capacity retention of 92.9% and a coulombic efficiency of 99.2% after 10,000 charge-discharge cycles, indicating its long-term reliability and performance in energy storage applications (Figure 9f). The superior performance of the symmetric device ZIF-8/CoP@C//ZIF-8/CoP@C can be linked to the significant porosity of ZIF-8 and the conductive nature of CoP@C, which facilitates rapid ion transport and improves the electrochemical behaviour.

Table 2 provides a comprehensive overview of the electrochemical characteristics of the ZIF-8/CoP@C composite in comparison to various other ZIF/carbon composite electrode materials. ZIF-8/polyaniline@cellulose-derived carbon aerogel using urea and KOH as activation and doping source delivered an E.D. of 13.4 and 81.8 Wh kg⁻¹ in 2 M KOH and Et₄NBF₄/AN electrolyte, respectively.^[74] The reason for such high E.D. in Et₄NBF₄/AN is that it is an organic liquid electrolyte and organic electrolytes provide a wider electrochemical stability window than aqueous electrolytes. This enhanced stability allows for higher operating voltages. However, they come with drawbacks such as high cost, volatility, and potential toxicity. The enhanced electrochemical performance of ZIF-8/CoP@C is chiefly a result of a well-designed pore structure and optimal nitrogen doping. In particular, the increased nitrogen concentration is significant because nitrogen atoms, being similar in size to carbon, can establish robust covalent bonds with carbon, thereby contributing to the material's superior performance. The improved electrochemical performance enhancement is a result of the synergistic effects between ZIF-8 and CoP@C, where the unique properties of both materials combine to enhance overall efficiency. This interaction leads to better conductivity, increased SSA, improved catalytic activity, and high cyclic stability, contributing to superior electrochemical performance.

4. Conclusion

This study presents a straightforward synthesis of the ZIF-8/CoP@C composite material, which is evaluated as a potential electrode material for SCs. The ZIF-8/CoP@C composite exhibits enhanced conductive pathways compared to the standalone ZIF-8. While ZIF-8 has a high SSA that facilitates efficient diffusion of electrolyte ions, it lacks sufficient conductive pathways, which limit charge transfer to the current collector. The combination of ZIF-8 and CoP@C integrates desirable properties such as high SSA, porosity, and electrical conductivity. The N-doping inherently present in the CoP@C functioned as a nucleation center for ZIF-8 growth and it significantly enhanced the electrochemical performance of the ZIF-8/CoP@C composite. Electrochemical assessments using both two and three-electrode systems have demonstrated that incorporating CoP@C into ZIF-8 leads to markedly superior electrochemical performance compared to the pure ZIF-8 electrode. The symmetrical supercapacitor device

achieved a remarkable E.D. of 25.7 Wh kg⁻¹ and a P.D. of 402.1 W kg⁻¹, alongside excellent cyclic stability. This composite's adjustable porosity and conductivity enhance its prospects as a candidate for energy storage.

Acknowledgments

The authors would like to thank the Director, NPL, for providing all research facilities and permission to publish results. The authors, P. S. and C. K. acknowledge CSIR, India, for providing financial support as a fellowship. The authors wish to extend their sincere gratitude to Mr. R.K. Seth, Mr. Naval Kishor Upadhyay, Dr. J.S. Tawale, Mr. Parveen Tanwar, and Mrs. Shweta for their invaluable assistance in material characterization. And authors would like to acknowledge the MNRF and RMMF facility, RMIT University.

Conflict of Interest

The authors declare no conflict of interest.

Author Contributions

Pinky Saharan: experimental, characterizations, and manuscript writing. **Chandan Kumar:** experimental and characterization. **Mandeep Singh:** data analysis and discussions. **Shashank Sundriyal:** conceptualization, data analysis, discussion, manuscript review. **Sanjay R. Dhakate:** project leader, conceptualization, manuscript review, and supervision.

Data Availability Statement

The authors confirm that the data supporting this study's findings are included in the article and its Supplementary Information. Additional data will be made available upon request.

Keywords: aqueous supercapacitors • copolymers • composites • energy density • zeolitic-imidazolate frameworks

- [1] C. Xiang, Y. Liu, Y. Yin, P. Huang, Y. Zou, M. Fehse, Z. She, F. Xu, D. Banerjee, D. H. Merino, A. Longo, H. B. Kraatz, D. F. Brougham, B. Wu, L. Sun, *ACS Appl. Energy Mater.* **2019**, *2*, 3389.
- [2] R. Warren, O. Andrews, S. Brown, F. J. Colón-González, N. Forstenhäusler, D. E. H. J. Gernaat, P. Goodwin, I. Harris, Y. He, C. Hope, D. Manful, T. J. Osborn, J. Price, D. Van Vuuren, R. M. Wright, *Clim. Change* **2022**, *172*, 1.
- [3] P. Svasta, R. Negriou, A. Vasile, in Proc.—2017 5th Int. Symp. Electr. Electron. Eng. ISEE. 2017, **2017**, pp. 1–5.
- [4] S. Wu, Y. Chen, T. Jiao, J. Zhou, J. Cheng, B. Liu, S. Yang, K. Zhang, W. Zhang, *Adv. Energy Mater.* **2019**, *9*, 1.
- [5] V. H. N. Martins, N. M. S. Siqueira, J. E. S. Fonsaca, S. H. Domingues, V. H. R. Souza, *ACS Appl. Nano Mater.* **2021**, *4*, 5553.
- [6] S. Khanna, P. Dubey, S. S. Sharda, P. H. Maheshwari, *Energy Fuels* **2024**, *38*, 17003.
- [7] S. R. Venna, M. A. Carreon, *J. Am. Chem. Soc.* **2010**, *132*, 76.
- [8] V. Shrivastav, S. Sundriyal, A. Kaur, U. K. Tiwari, S. Mishra, A. Deep, *J. Alloys Compd.* **2020**, *843*, 155992.
- [9] N. Cheng, L. Ren, X. Xu, Y. Du, S. X. Dou, *Adv. Energy Mater.* **2018**, *8*, 1.

- [10] B. Chen, Z. Yang, Y. Zhu, Y. Xia, *J. Mater. Chem. A* **2014**, *2*, 16811.
- [11] S. Kouser, A. Hezam, M. J. N. Khadri, S. A. Khanum, *J. Porous Mater.* **2022**, *29*, 663.
- [12] A. Kaur, V. Shrivastav, P. Dubey, A. Deep, I. Mudahar, S. Sundriyal, S. Mishra, *Energy Fuels* **2023**, *37*, 11376.
- [13] C. Ruan, D. Zhu, J. Qi, Q. Meng, F. Wei, Y. Ren, Y. Sui, H. Zhang, *Surf. Interfaces* **2021**, *25*, 101274.
- [14] H. Wang, Q. He, S. Liang, Y. Li, X. Zhao, L. Mao, F. Zhan, L. Chen, *Energy Storage Mater.* **2021**, *43*, 531.
- [15] D. Kim, D. W. Kim, W. G. Hong, A. Coskun, *J. Mater. Chem. A* **2016**, *4*, 7710.
- [16] A. G. Yeklangi, F. Rahimi, S. Akbari, *J. Nanosci. Technol.* **2021**, *3*, 1.
- [17] L. Wan, E. Shamsaei, C. D. Easton, D. Yu, Y. Liang, X. Chen, Z. Abbasi, A. Akbari, X. Zhang, H. Wang, *Carbon N. Y.* **2017**, *121*, 330.
- [18] S. Sundriyal, V. Shrivastav, H. Kaur, S. Mishra, A. Deep, *ACS Omega* **2018**, *3*, 17348.
- [19] D. Kumar, A. Joshi, G. Singh, R. K. Sharma, *Chem. Eng. J.* **2022**, *431*, 134085.
- [20] E. Samuel, B. Joshi, C. Park, A. Aldalbahi, M. Rahaman, S. S. Yoon, *Electrochim. Acta* **2020**, *362*, 137154.
- [21] W. Zhang, Y. Tan, Y. Gao, J. Wu, J. Hu, A. Stein, B. Tang, *J. Appl. Electrochem.* **2016**, *46*, 441.
- [22] A. Hosseiniyan, A. H. Amjad, R. Hosseinzadeh-Khanmiri, E. Ghorbani-Kalhor, M. Babazadeh, E. Vessally, *J. Mater. Sci. Mater. Electron.* **2017**, *28*, 18040.
- [23] D. Wang, Y. Chen, H. Wang, P. Zhao, W. Liu, Y. Wang, *J. Yang, Appl. Surf. Sci.* **2018**, *457*, 1018.
- [24] C. Jin, T. C. Nagaiah, W. Xia, B. Spliehoff, S. Wang, M. Bron, W. Schuhmann, M. Muhler, *Nanoscale* **2010**, *2*, 981.
- [25] A. Zhao, J. Masa, M. Muhler, W. Schuhmann, W. Xia, *Electrochim. Acta* **2013**, *98*, 139.
- [26] P. Saharan, M. Singh, C. Kumar, S. Sundriyal, S. R. Dhakate, *ACS Appl. Nano Mater.* **2023**, *6*, 21909.
- [27] Q. Abbas, R. Raza, I. Shabbir, A. G. Olabi, *J. Sci.: Adv. Mater. Devices* **2019**, *4*, 341.
- [28] S. Yin, X. Bai, D. Jiang, L. Liao, H. Liu, *J. Mater. Chem. A* **2024**, *12*, 23243.
- [29] D. Zhu, K. Cheng, Y. Wang, D. Sun, L. Gan, T. Chen, J. Jiang, M. Liu, *Electrochim. Acta* **2017**, *224*, 17.
- [30] S. Jadoun, U. Riaz, *Polym. Technol. Mater.* **2020**, *59*, 484.
- [31] W. Lu, S. Yin, X. Wu, Q. Luo, E. Wang, L. Cui, C. Y. Guo, *J. Mater. Chem. C* **2021**, *9*, 2898.
- [32] T. Ma, M. Liu, N. A. O. Offiong, J. Duan, Y. Liu, H. Ren, R. Zhou, *J. Hazard. Mater.* **2023**, *445*, 130580.
- [33] Q. Liu, H. Li, X. Cui, X. Liu, X. Zhang, Y. Yang, *React. Funct. Polym.* **2019**, *144*, 104349.
- [34] M. Bhaumik, A. Maity, V. V. Srinivasu, M. S. Onyango, *Chem. Eng. J.* **2012**, *181-182*, 323.
- [35] P. Saharan, M. Singh, A. Gupta, C. Kumar, S. Sundriyal, S. R. Dhakate, *J. Energy Storage* **2023**, *73*, 108928.
- [36] C. Kumar, A. Gupta, P. Saharan, M. Singh, S. R. Dhakate, *Diam. Relat. Mater.* **2023**, *140*, 110433.
- [37] P. Dubey, V. Shrivastav, A. Kaur, P. H. Maheshwari, S. Sundriyal, *Energy and Fuels* **2022**, *36*, 626.
- [38] S. Yang, N. Xia, M. Li, P. Liu, *RSC Adv.* **2019**, *9*, 15217.
- [39] A. Schejn, A. Aboulach, L. Balan, V. Falk, J. Lalevée, G. Medjahdi, L. Aranda, K. Mozet, R. Schneider, *Catal. Sci. Technol.* **2015**, *5*, 1829.
- [40] J. Cravillon, S. Münzer, S. J. Lohmeier, A. Feldhoff, K. Huber, M. Wiebcke, *Chem. Mater.* **2009**, *21*, 1410.
- [41] Z. Ma, J. Li, R. Ma, J. He, X. Song, Y. Yu, Y. Quan, G. Wang, *New J. Chem.* **2022**, *46*, 7230.
- [42] E. G. Masibi, T. A. Makhetha, R. M. Moutloali, *Membranes (Basel)* **2022**, *12*, 436.
- [43] C. Kumar, T. I. Singh, P. Saharan, A. Gupta, J. Singh, M. Singh, S. R. Dhakate, *FlatChem* **2024**, *46*, 100689.
- [44] J. Liang, C. Xiang, Y. Zou, X. Hu, H. Chu, S. Qiu, F. Xu, L. Sun, *J. Mater. Sci. Technol.* **2020**, *55*, 190.
- [45] Y. Xiao, B. Guo, J. Zhang, C. Hu, R. Ma, D. Wang, J. Wang, *Dalton Trans.* **2020**, *49*, 5730.
- [46] C. Gao, P. Wang, Z. Wang, S. K. Kær, Y. Zhang, Y. Yue, *Nano Energy* **2019**, *65*, 104032.
- [47] J. Gu, L. Sun, Y. Zhang, Q. Zhang, X. Li, H. Si, Y. Shi, C. Sun, Y. Gong, Y. Zhang, *Chem. Eng. J.* **2020**, *385*, 123454.
- [48] M. Ghafoor, Z. U. Khan, M. H. Nawaz, N. Akhtar, A. Rahim, S. Riaz, *Environ. Monit. Assess.* **2023**, *195*, 423.
- [49] C. Lv, W. Kang, S. Liu, P. Yang, Y. Nishina, S. Ge, A. Bianco, B. Ma, *ACS Nano* **2022**, *16*, 11428.
- [50] T. Van Ngo, M. Moussa, T. T. Tung, C. Coghlann, D. Losic, *Electrochim. Acta* **2020**, *329*, 135104.
- [51] Y. Hua, J. Mai, R. Su, C. Ma, J. Liu, C. Zhao, Q. Zhang, C. Liao, Y. Wang, *Biosensors* **2024**, *14*, 617.
- [52] L. Guan, D. Li, S. Ji, X. Wei, F. Meng, *Materials (Basel)* **2025**, *18*, 1.
- [53] P. N. B. Rebecca, D. Durgalakshmi, S. Balakumar, R. A. Rakkes, *Chem. Eng. J.* **2024**, *484*, 149789.
- [54] X. Wei, Y. Wang, Y. Huang, C. Fan, *J. Alloys Compd.* **2019**, *802*, 467.
- [55] C. Hu, Y. C. Huang, A. L. Chang, M. Nomura, *J. Colloid Interface Sci.* **2019**, *553*, 372.
- [56] A. P. M. Udayan, O. Sadak, S. Gunasekaran, *ACS Appl. Energy Mater.* **2020**, *3*, 12368.
- [57] N. T. Bui, H. Kang, S. J. Teat, G. M. Su, C. W. Pao, Y. S. Liu, E. W. Zaia, J. Guo, J. L. Chen, K. R. Meihaus, C. Dun, T. M. Mattox, J. R. Long, P. Fiske, R. Kostecki, J. J. Urban, *Nat. Commun.* **2020**, *11*, 1.
- [58] S. Luanwuthi, A. Krittayavathananon, P. Srimuk, M. Sawangphruk, *RSC Adv.* **2015**, *5*, 46617.
- [59] Q. Liu, X. Gao, Z. Liu, L. Gai, Y. Yue, H. Ma, *Materials (Basel)* **2023**, *16*, 3378.
- [60] Y. Wang, Y. Liu, D. Wang, C. Wang, L. Guo, T. Yi, *Appl. Surf. Sci.* **2020**, *506*, 145014.
- [61] M. Mirzaeian, Q. Abbas, D. Gibson, M. Mazur, *Energy* **2019**, *173*, 809.
- [62] S. Feng, X. Jia, J. Yang, Y. Li, S. Wang, H. Song, *J. Mater. Sci. Mater. Electron.* **2020**, *31*, 22534.
- [63] T. P. Mofokeng, Z. N. Tetana, K. I. Ozoemena, *Carbon N. Y.* **2020**, *169*, 312.
- [64] X. Mao, Y. Zou, F. Xu, L. Sun, H. Chu, H. Zhang, J. Zhang, C. Xiang, *ACS Appl. Mater. Interfaces* **2021**, *13*, 22664.
- [65] L. Han, K. G. Karthikeyan, M. A. Anderson, K. B. Gregory, *J. Colloid Interface Sci.* **2014**, *430*, 93.
- [66] X. Liu, C. Ma, Y. Wen, X. Chen, X. Zhao, T. Tang, R. Holze, E. Mijowska, *Carbon N. Y.* **2021**, *171*, 819.
- [67] P. Saharan, M. Singh, C. Kumar, S. Sundriyal, S. R. Dhakate, *ACS Appl. Nano Mater.* **2023**, *6*, 21909.
- [68] E. E. Sann, Y. Pan, Z. Gao, S. Zhan, F. Xia, *Sep. Purif. Technol.* **2018**, *206*, 186–191.
- [69] M. Singh, A. Gupta, P. Saharan, C. Kumar, S. R. Dhakate, *J. Energy Storage* **2023**, *67*, 107617.
- [70] P. Pandey, S. Bhowmick, M. Qureshi, *ACS Appl. Mater. Interfaces* **2023**, *15*, 39435.
- [71] J. Wang, J. Polleux, J. Lim, B. Dunn, *J. Phys. Chem. C* **2007**, *111*, 14925.
- [72] P. Dubey, V. Shrivastav, M. Jain, K. K. Pant, P. H. Maheshwari, S. Sundriyal, *Energy Fuels* **2023**, *37*, 8659.
- [73] M. Singh, A. Gupta, S. Sundriyal, K. Jain, S. R. Dhakate, *Mater. Chem. Phys.* **2021**, *264*, 124454.
- [74] M. Shang, X. Zhang, J. Zhang, J. Sun, X. Zhao, S. Yu, X. Liu, B. Liu, X. Yi, *Carbohydr. Polym.* **2021**, *262*, 117966.
- [75] J. Wu, X. Zhang, F. Wei, Y. Sui, J. Qi, *Mater. Lett.* **2020**, *258*, 2.
- [76] C. Cai, Y. Zou, C. Xiang, H. Chu, S. Qiu, Q. Sui, F. Xu, L. Sun, A. Shah, *Appl. Surf. Sci.* **2018**, *440*, 47.
- [77] L. Wan, J. Wei, Y. Liang, Y. Hu, X. Chen, E. Shamsaei, *RSC Adv.* **2016**, *6*, 76575.
- [78] Y. Liu, Q. Sui, Y. Zou, C. Xiang, F. Xu, J. Xie, L. Sun, *Int. J. Electrochem. Sci.* **2016**, *14*, 5096.
- [79] S. Yetiman, F. K. Dokan, M. S. Onses, E. Yilmaz, E. Sahmetlioglu, *Int. J. Energy Res.* **2022**, *46*, 22730.
- [80] C. Guo, G. Li, Y. Wu, X. Wang, Y. Niu, J. Wu, *Energies (Basel)* **2023**, *16*, 7232.

Manuscript received: June 22, 2025

Revised manuscript received: August 10, 2025

Version of record online: